Journal of Rock Mechanics and Geotechnical Engineering 18 (2026) 3934–3948

Contents lists available at ScienceDirect

Journal of Rock Mechanics and Geotechnical Engineering

journal homepage: www.jrmge.cn

Full Length Article

Characterizing soil shrinkage and soil-water retention behaviors of clayey soils with pore-size distribution and microstructure evolution

Sheng'ao Jia [a,b], De'an Sun [a,*], Pan Chen [b,c,**]

[a] Department of Civil Engineering, Shanghai University, 99 Shangda Road, Shanghai, 200444, China
[b] State Key Laboratory of Geomechanics and Geotechnical Engineering Safety, Institute of Rock and Soil Mechanics, Chinese Academy of Sciences, Wuhan, 430071, China
[c] University of Chinese Academy of Sciences, Beijing, 100049, China

ARTICLE INFO

Article history:
Received 7 February 2025
Received in revised form
24 June 2025
Accepted 23 July 2025
Available online 5 August 2025

Keywords:
Clayey soil
Soil shrinkage
Soil-water retention
Pore-size distribution
Microstructure

ABSTRACT

The soil-water retention and soil shrinkage characteristics are both crucial constitutive relations for unsaturated soils. Although existing research has explored the correlation between these two characteristics to some extent, the underlying mechanisms remain inadequately investigated. To investigate the correlation between the soil-water retention and soil shrinkage behavior, a series of soil-water retention and soil shrinkage tests is performed on compacted clays over a wide suction range (0–367 MPa). The test results show that the pore water in compacted clays is first expelled from large pores in low suction range. The drainage of pore water at low suctions is predominantly responsible for the phase of structural shrinkage in the soil shrinkage curve. The consistency between the characteristic transitional water contents in the soil shrinkage curve (SSC) and the inflection points in the soil-water retention curve (SWRC) is identified for all the compacted clays. The bimodal pore-size distributions (PSDs) of different clayey soils are obtained using the mercury intrusion porosimetry. The bimodal pore-size distribution characterization is the intrinsic factor in shaping the bimodal morphology in the SWRC over a wide suction range. The low proportion of micropores in clays is responsible to the indistinct zero-shrinkage stage of the SSC. The microstructure measured by the scanning electron microscope indicates the manifestation of aggregation effects during desaturation process. The results demonstrate that soil shrinkage is primarily caused by the contraction of inter-aggregate pores, rather than the evolution of intra-aggregate pores. The findings can greatly enhance the understanding of the soil-water retention and mechanical behavior of compacted clays in varying water content conditions.

1. Introduction

In arid and semi-arid regions, the water in clayey soils can be expelled from the pores under the interaction with the atmosphere, resulting in soil shrinkage deformation (Haines, 1923; Fredlund et al., 2002). Soil shrinkage can lead to ground settlement and soil cracking, which results in damage of surface structures, such as soil slope, dam, and building foundation (Leroueil, 2001; Marinho, 2018). Revealing the mechanisms behind soil shrinkage is crucial to developing methods that can prevent or retard the degradation of these earthen structures.

Soil shrinkage refers to the phenomenon where the volume and pore structure of soil respond to changes in water content. The soil shrinkage and soil-water retention have become the fundamental constitutive relationships in geotechnical engineering and agriculture (Peng and Horn, 2005; Fredlund, 2019). A number of studies have been performed on the characteristics of soil-water retention and soil shrinkage individually. Although the connection between soil shrinkage and soil-water retention behaviors has been identified (Lin and Cerato, 2013; Saha and Sekharan, 2021), the interaction mechanism between them has not been thoroughly investigated.

* Corresponding author. Department of Civil Engineering, Shanghai University, 99 Shangda Road, Shanghai, 200444, China.
** Corresponding author. State Key Laboratory of Geomechanics and Geotechnical Engineering Safety, Institute of Rock and Soil Mechanics, Chinese Academy of Sciences, Wuhan, 430071, China.
E-mail addresses: sundean@shu.edu.cn (D. Sun), pchen@whrsm.ac.cn (P. Chen).
Peer review under responsibility of Institute of Rock and Soil Mechanics, Chinese Academy of Sciences.

https://doi.org/10.1016/j.jrmge.2025.07.002

The factors influencing the soil-water retention behavior have been extensively studied. These include soil type, initial dry density, initial water content, and suction history (Sun et al., 2014; Chen et al., 2017). The soil-water retention behavior is generally characterized by the soil-water retention curve (SWRC). Common techniques for determining the SWRC of soils include the axis translation technique (ATT) in the range of 0–1.5 MPa, filter paper method, humidity control method, and chilled-mirror hygrometer method (Lu and Likos, 2004; Wei and Dewoolkar, 2006; Wayllace and Lu, 2012; Chen et al., 2017). However, the change in suction of silty and sandy soils is typically in a low suction range, and is less than approximately 0.5 MPa. In contrast, the suction range of cohesive soils, particularly for expansive soils, is much wider and can reach several hundred MPa (Gao and Sun, 2017; Ma et al., 2020; Chen et al., 2023). Hence, it is challenging to determine the SWRC of a clayey soil over a wide suction range using only one technique. Researchers commonly employ a combination of different measurement methods to determine the soil-water retention characteristics of soils within a wide suction range (e.g. 0–367 MPa) (Salager et al., 2013). Although several works have been performed to investigate the SWRC of clayey soils over a wide suction range (Salager et al., 2013; Gao and Sun, 2017), the comprehensive soil-water retention data covering both low and high suction ranges are quite limited due to technical limitations and time-consuming process. Hence, a comprehensive investigation on the SWRC of clayey soil is needed across the full suction range, especially in the high suction range for the primary shrinkage phase of clayey soil.

Soil shrinkage behavior is usually represented by the soil shrinkage curve (SSC). There are different techniques to determine the soil shrinkage data of a clayey soil, including the direct method, indirect method, and non-contact method. The direct method entails utilizing tools such as a vernier caliper to measure the sizes of soil specimens directly (e.g. Krisdani et al., 2008). Conversely, the indirect method, also known as the volume displacement method, involves determining the soil volume by sealing the soil with a liquid paraffin or a balloon. The change in volume of the liquid or balloon is then calculated to determine the volume change of the soil (e.g. Gupt et al., 2022). The non-contact method, employed to ascertain soil volume, eliminates the need for physical contact with a soil specimen. This is achieved through the application of technologies such as digital image processing or laser scanning, ensuring that the soil specimen remains undisturbed and undamaged (e.g. White et al., 2003; Jain et al., 2015; Jia et al., 2024). The literature has shown that the soil shrinkage properties are closely related to the basic physical index of clayey soil on the macroscale (Chen and Lu, 2018; Zhou and Lu, 2021). The evolution mechanism underlying the connection between the soil shrinkage and soil-water retention behaviors in macroscale may be unveiled by the evolution of soil structure in microscale (Jia et al., 2024). Currently, the microstructure of soil can be analyzed through some advanced testing techniques, such as the mercury intrusion porosimetry (MIP), X-ray computed tomography (X-CT), scanning electron microscope (SEM), electromagnetic methods (EM), dielectric spectroscopy, and nuclear magnetic resonance (NMR) (Tian et al., 2014; Schwing, 2016; Mishra, 2020; Yin et al., 2022; Wang et al., 2023; Zhang et al., 2023; Jia et al., 2024). The measured data from the microscopic tests can be used to explain and analyze the evolution of pore water in soils under different suction conditions (Schwing et al., 2014; Tian et al., 2018; Mishra, 2020; Tian and Wei, 2020; Bore et al., 2021; Wen et al., 2021). Researchers have developed the EM testing technique to investigate the coupled behavior of soil-water retention, shrinkage, and dielectric properties in fine-grained soils (Schwing et al., 2014; Schwing, 2016; Mishra et al., 2018; Bore et al., 2021). These experimental results have subsequently led to the development of corresponding theoretical models, thereby providing fresh insights on the multiphysical coupling behavior of soils during the desiccation process. The techniques are also utilized to study the influence of soluble salts on the soil shrinkage characteristics (Ma et al., 2020; Yao et al., 2021; Song et al., 2023, 2024). However, the connections among soil shrinkage, soil-water retention, and evolutions of pore-size distribution (PSD) and microscopic structure in clayey soil are rarely explored and quantitatively analyzed. Comprehensive understanding of the correlation between these soil behaviors during the process of water loss holds significant theoretical implications. Not only does it reveal the intrinsic mechanisms behind hydraulic behavior or in this process, but it also provides a theoretical foundation for practical applications in geotechnical engineering.

In this study, a series of soil-water retention and soil shrinkage tests was conducted on various compacted clayey soils over a wide suction range. From saturated state to quite low water content state in clayey soils, the evolutions of the soil-water retention and soil shrinkage behavior were observed and explored in detail. Compared to the measured data of SWRC and SSC, the connection between the soil-water retention and soil shrinkage was carefully investigated. Furthermore, using the MIP and SEM techniques, the evolutions of pore structures in clayey soils under drying conditions were determined at the same water content state as the measured SWRC and SSC. Finally, the evolutions of the PSD and microstructure were used to elucidate the underlying mechanism of the correlation between the soil-water retention and soil shrinkage characteristics.

2. Materials and methods

2.1. Specimen preparation

Six types of clayey soils obtained from the fields in Yunnan, Guilin, Longsheng, Yueyang, Sanmenxia and Taizhou in China were used to determine the soil shrinkage and soil-water retention data over a wide suction range. First, the basic physical properties of the clays are determined according to the ASTM standards. The specific gravity (G_S) and Atterberg limits of clayey soils are determined based on ASTM D854-23 (2023) and ASTM D4318-17e1 (2018). The basic physical properties of the clays are summarized in Table 1. The grain-size distributions of six clays are determined following ASTM D7928-21e1 (2021), as shown in Fig. 1a and Table 1 (Jia et al., 2024). According to ASTM D2487-17e1 (2018), the six clayey soils are classified into two categories: high plasticity (MH) and low plasticity clay (CL). The plasticity chart is shown in Fig. 1b. From Table 1, the highest clay content occurs in Yunnan clay and Guilin clay, whereas the lowest clay content is found in Sanmenxia clay.

Fig. 2 provides the mineral compositions and their proportions of different clays obtained by X-ray diffraction method (ASTM F3419-22, 2022). From Fig. 2, the iron oxide content exceeds 10 % in Yunnan clay, Guilin clay, and Longsheng clay. Among the three high-plasticity clays, Longsheng clay possesses the highest iron oxide content. Compared to the three low-plasticity clays, the high-plasticity clays have a higher plastic limit (PL) and liquid limit (LL), as listed in Table 1. One of the reasons for the higher Atterberg limits is that the free iron oxide in clay can enhance the plasticity of clays. Furthermore, the three high-plasticity clays possess higher contents of kaolinite and illite, while the three low-plasticity clays have higher contents of illite and illite/smectite mixed layer (I/S) (Moore and Reynolds, 1997). The proportion of these clay minerals in soils significantly influences their swelling potential and plasticity.

Table 1
Physical indices of clayey soils.

Index		Yunnan clay	Guilin clay	Longsheng clay	Yueyang clay	Sanmenxia clay	Taizhou clay
USCS		MH	MH	MH	CL	CL	CL
G_s		2.82	2.8	2.88	2.76	2.74	2.78
Atterberg limits	PL (%)	36.8	37.7	46.8	24.1	20	21
	LL (%)	62.7	66.1	77.7	47.9	37	46.3
	PI (%)	25.9	28.4	30.9	23.8	17	25.3
Grain-size distribution	>0.075 mm (%)	0	0	0	0	0	0
	≤0.075 mm, >0.002 mm (%)	51.62	32.81	66.21	65.33	89.37	66.44
	≤0.002 mm (%)	48.38	67.19	33.79	34.67	10.62	33.56

Note: USCS represents the unified soil classification system, G_s denotes the specific gravity of soil, and PI is the plastic index of soil.

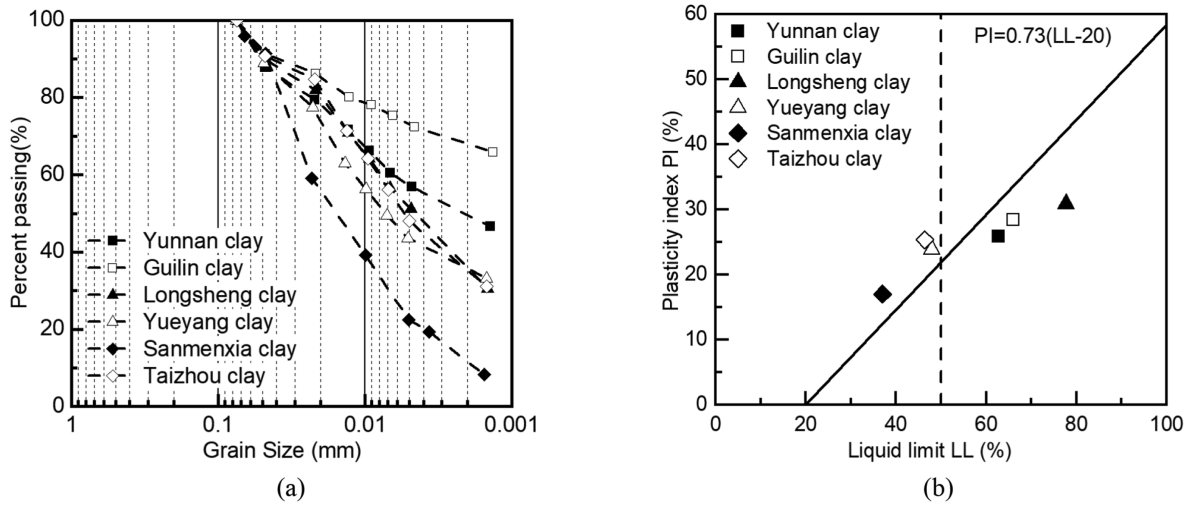

Fig. 1. The grain-size distributions (a) and plasticity chart (b) of the six clays used in this study.

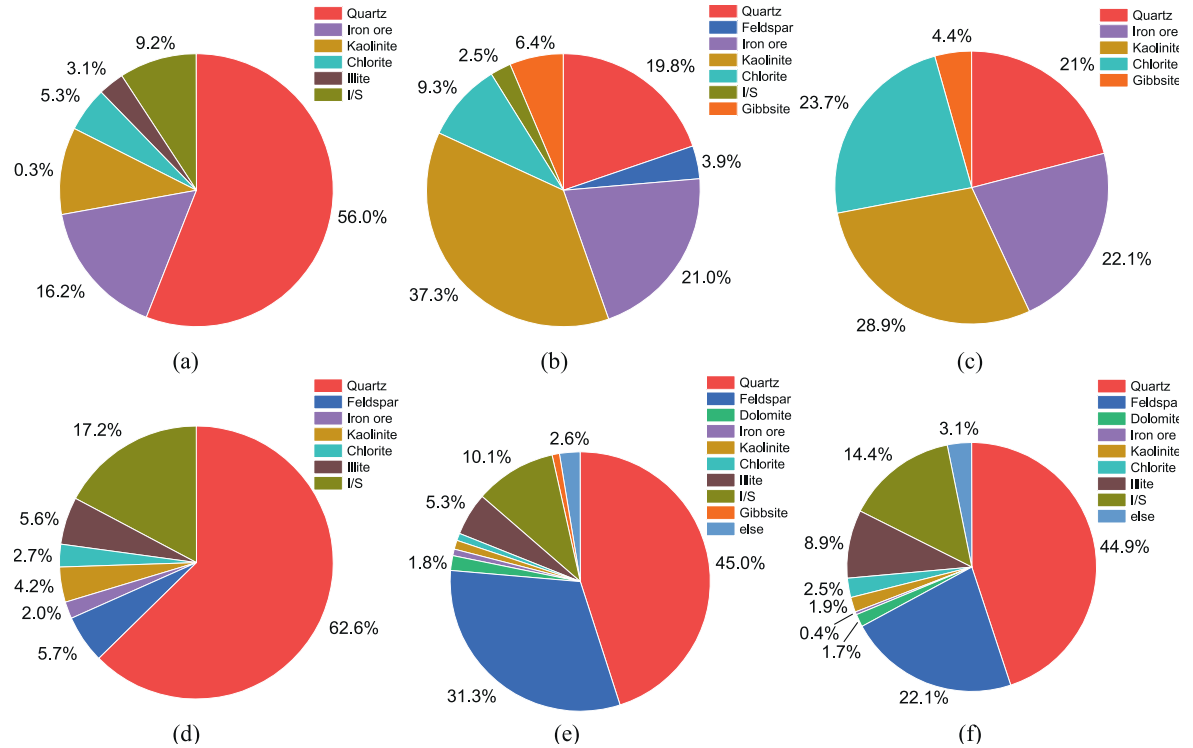

Fig. 2. Mineral components for tested clayey soils: (a) Yunnan clay, (b) Guilin clay, (c) Longsheng clay, (d) Yueyang clay, (e) Sanmenxia clay, and (f) Taizhou clay.

The initial dry density and initial water content of the specimens for the six clays are determined under in situ conditions, with specific values detailed in Table 2. The initial dry densities of all specimens are controlled using the static compaction method with the given initial water content. All specimens are saturated using the vacuum saturation method (Gao and Sun, 2017).

The image processing techniques are employed to determine the SSCs of compacted clays during drying processes (Jia et al., 2024). On this basis, the SWRCs and microstructural PSD patterns of identically conditioned soils are examined. In this study, the SWRCs over a wide suction range are obtained using the transient water release and imbibition method (TRIM) system based on the ATT, and the water potential meter WP4C, which is based on the dew point method. The specimens for the TRIM system are prepared with a diameter of 54 mm and a height of 30 mm (Chen et al., 2017). For the water potential measurement with WP4C device, the diameter and height of the test specimens are 35 mm and 8 mm, respectively.

2.2. Test equipment

Combining ATT and dew point method, the SWRCs of six clayey soils are determined over a wide suction range (0–367 MPa). The schematic diagrams of the test equipment used for measuring the SWRC are shown in Fig. 3. In the low suction range (0–500 kPa), the SWRC is obtained under each suction equilibrium state using the ATT (Lu and Likos, 2004; Lu et al., 2006; Chen et al., 2017), as shown in Fig. 3a. In view of the extended testing duration and increased error probability correlated with water extraction at the suctions exceeding 500 kPa in the ATT, this study restricts the applied suctions up to 300 kPa. For the intermediate to high suction range, the SWRCs are determined using the WP4C device (Ma et al., 2020), as depicted in Fig. 3b. At low suction, the testing system comprises a gas supply system, a specimen chamber, a bubble flushing device, a balance, and a data acquisition system. The gas supply system consists of a gas supply device and pressure-regulator with different ranges. The specimen chamber consists of a cutting ring, a ceramic plate with the high entry value of 500 kPa, sealing rings, and upper and lower chambers, as shown in Fig. 3a. The measurement range of the WP4C device is 0–300 MPa, with an accuracy of $\pm$50 kPa. It has the potential to produce a relatively low value which may coincide with the results obtained from the ATT. Within this overlapping range, the reliability and validity of various testing methods, including the ATT, chilled-mirror dewpoint method, and filter paper method, require further investigation in future studies. The WP4C system includes the cold-mirror sensor, the relative humidity (RH) sensor, the sample chamber, and the data acquisition part, as shown in Fig. 3b.

2.3. Test procedures

After saturation, the SWRCs of the soil specimens are determined using the test devices TRIM and WP4C shown in Fig. 3. The measuring procedures for the SWRC are shown in Fig. 4, and are described in detail as follows:

(1) Low suction range: The saturated ceramic plate is first placed in the specimen chamber, and the pipelines connecting the specimen and the outflow box are saturated by flushing the deionized water through the bubble flushing device. Then, the saturated specimen is placed on the ceramic plate in the specimen chamber. The bolts are used to fix the bottom and top of the chamber to prevent air leakage. In this study, the steady-state multi-step outflow method is employed to determine the SWRC at the low suction (Chen et al., 2017). The air pressure is applied in stepwise increases according to the drainage processes. The next pressure is applied when the equilibrium condition in the specimen is reached in the current pressure step. The standard for the equilibrium condition is that the outflow water content is less than 0.01 g within 4 h (Chen et al., 2017). This process continues until the water content essentially ceases to be expelled, marking the end of the tests. It is noted that the first level of the applied suction should correspond to the air-entry value of the soil specimen in the SWRC testing, which is influenced by the soil type and dry density. The applied air pressure in the first step needs to be determined with caution to avoid the effects of air entrapment (Chen et al., 2015, 2017).

(2) High suction range: The SWRC data at high suctions are measured by following the standard ASTM D6836-16 (2016). A staged desaturation method is used to measure the water content of a tested specimen under the controlled desaturation rate. The RH method is employed using desiccators containing saturated salt solutions to provide stable RH environments, with each salt type generating a specific RH level. The desiccators are employed to control the desorption process of soil specimens, ensuring that the specimens are not in direct contact with the solutions. The test temperature is consistently maintained at 25 °C. To regulate the desorption rate and obtain a wider suction range of data points, five distinct salts ($ZnSO_4$, K_2CO_3, $MgCl_2$, LiCl, and LiBr) are selected as solutes for the supersaturated solutions. These solutions provide RH levels of approximately 90 %, 43.2 %, 32.6 %, 11.3 %, and 6.4 %, respectively. The corresponding equilibrium suction values, calculated using the Kelvin equation, are approximately 14.6, 116.4, 155.2, 302.4, and 382.2 MPa under the room temperature (Lu and Likos, 2004; ASTM E104-20a, 2020). It is noteworthy that no salts are added to the soil specimens. Hence, osmotic suction is considered negligible, and the total suction is assumed to be equivalent to matric suction. Initially, the saturated specimen is placed in a drying chamber containing an oversaturated salt solution at the bottom, as shown in Fig. 4. After the loss mass of pore water reaches 0.2–0.3 g for each stage, the specimen is taken out and put in a sealed chamber for more than 24 h (ASTM D6836-16, 2016). After the equilibrium state is reached, the suction of the soil

Table 2
Initial conditions for preparing compacted clays.

No.	Soil type	Water content (%)	Dry density (g/cm^3)	Void ratio	Porosity
1	Yunnan clay	15	1.25	1.27	0.56
2	Guilin clay	15	1.25	1.31	0.57
3	Longsheng clay	20	1.15	1.61	0.62
4	Yueyang clay	15	1.4	1.02	0.5
5	Sanmenxia clay	12	1.5	0.84	0.46
6	Taizhou clay	15	1.4	1.03	0.51

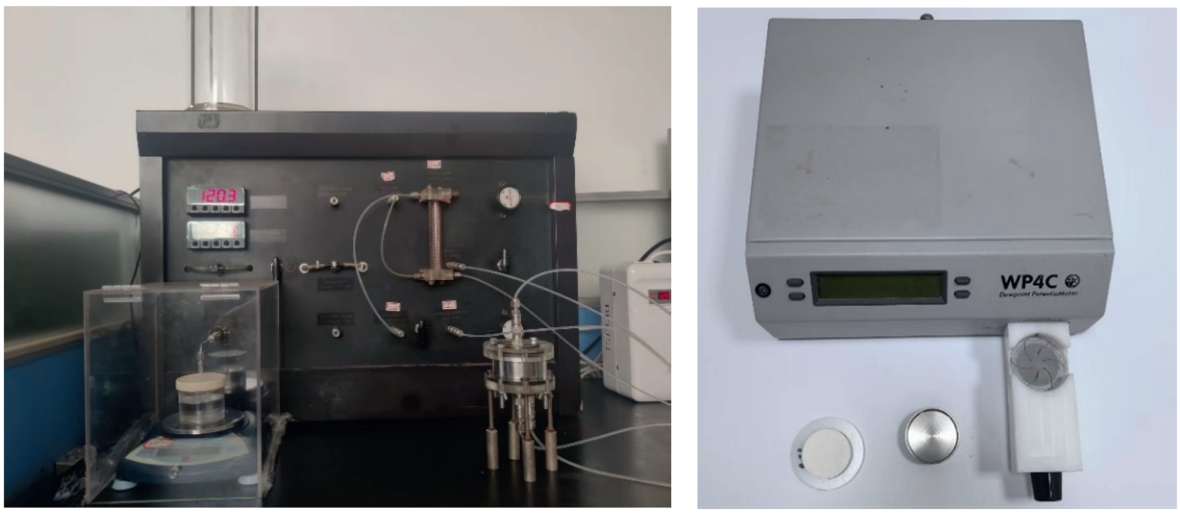

Fig. 3. The equipment for determining the SWRCs of clayey soils: (a) TRIM for SWRC at low suction, and (b) WP4C for SWRC at high suction.

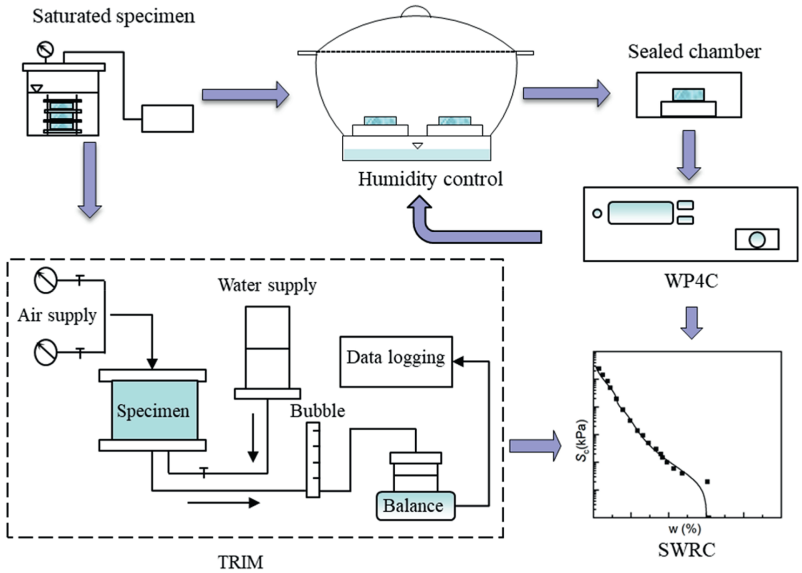

Fig. 4. Flowchart for the measuring procedures of SWRC.

specimen is measured using the WP4C device. The desaturation continues in the drying chamber until the completely dry state is reached.

2.4. Soil shrinkage measurement

The SSCs are obtained using image analysis techniques in this study. The specimen surface area is determined from photographs (Fig. 5a), and the specimen height is gauged with a dial indicator (Fig. 5b). Desiccation is conducted in sealed chambers housing supersaturated salt solutions to maintain controlled RH environments. This method enables the acquisition of a complete shrinkage curve from a single specimen without causing structural damage. The comprehensive testing methodology for the SSCs is detailed in Jia et al. (2024).

2.5. Microstructure investigation

A series of MIP and SEM analyses is conducted on clay specimens with varying degrees of saturation. The objective of this study is to determine the PSD and microscopic structure of different clays during the drying process. To characterize the structure evolution under drying conditions, the PSD and microscopic structure of the specimens with the same soil-water state as the SWRC and SSC measurements are determined, respectively.

Since both MIP and SEM tests require the use of dried specimens, appropriate dying methods are employed before testing. Conventional drying techniques such as oven or air drying can change the soil's pore structure. However, freeze-drying, based on the principle of ice sublimation, avoids the formation of air-water interfaces and prevents soil shrinkage due to water content

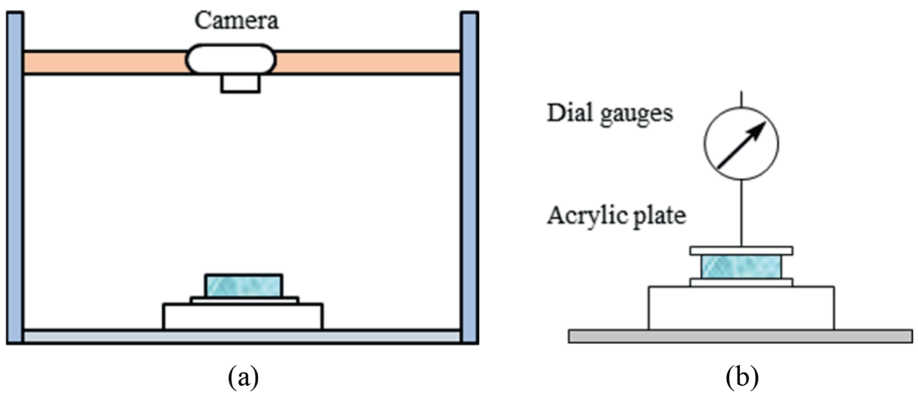

Fig. 5. Equipment for measuring SSC: (a) Photographic platform for radial deformation measurement, and (b) Dial indicator for height measurement.

fluctuations, thereby preserving the original microstructure of specimens. To preserve the microstructural pore characteristics and ensure rapid freezing of pore water, the specimens are initially flash-frozen in liquid nitrogen for over 1 h. Subsequently, these frozen specimens are transferred to a freeze dryer (Fig. 6a) and dried following the operating manual. Once the freeze-drying process is completed, the specimens are retrieved for subsequent MIP and SEM analyses (Gillott, 1976; Shi et al., 1999; Mitchell and Soga, 2005).

The MIP is a physical testing method for measuring the pore structure of materials. The fundamental principle underpinning the MIP test is Washburn's equation:

$$D = -\frac{4\gamma \cos\theta}{P} \tag{1}$$

where D is the pore diameter, γ is the mercury surface tension (0.484 N/m at 25 °C), θ is the contact angle between the liquid mercury and the solid surface (140°), and P is the pressure required to inject mercury. Mercury is a hydrophobic material that is not easily infiltrated into the soil naturally. Under a pressure P, mercury will be squeezed into material pores. The smaller the pore diameter, the greater the pressure required for mercury to enter the pore. According to Eq. (1), the pore size can be calculated, and then the complete PSD can be obtained.

The MIP testing equipment is shown in Fig. 6b. The freeze-dried soil sample is placed into the equipment and the testing is conducted to obtain cumulative mercury injection curve and then PSD. This study tests the PSD of six types of soils in a saturated state. Prior to the SEM observation, the freeze-dried specimens are gold-coated to enhance conductivity and then examined using the SEM apparatus, as shown in Fig. 6c. Subsequently, the specimens are scanned using the SEM equipment to obtain surface images. Adjusting the magnification allows for scanning photos at different scales.

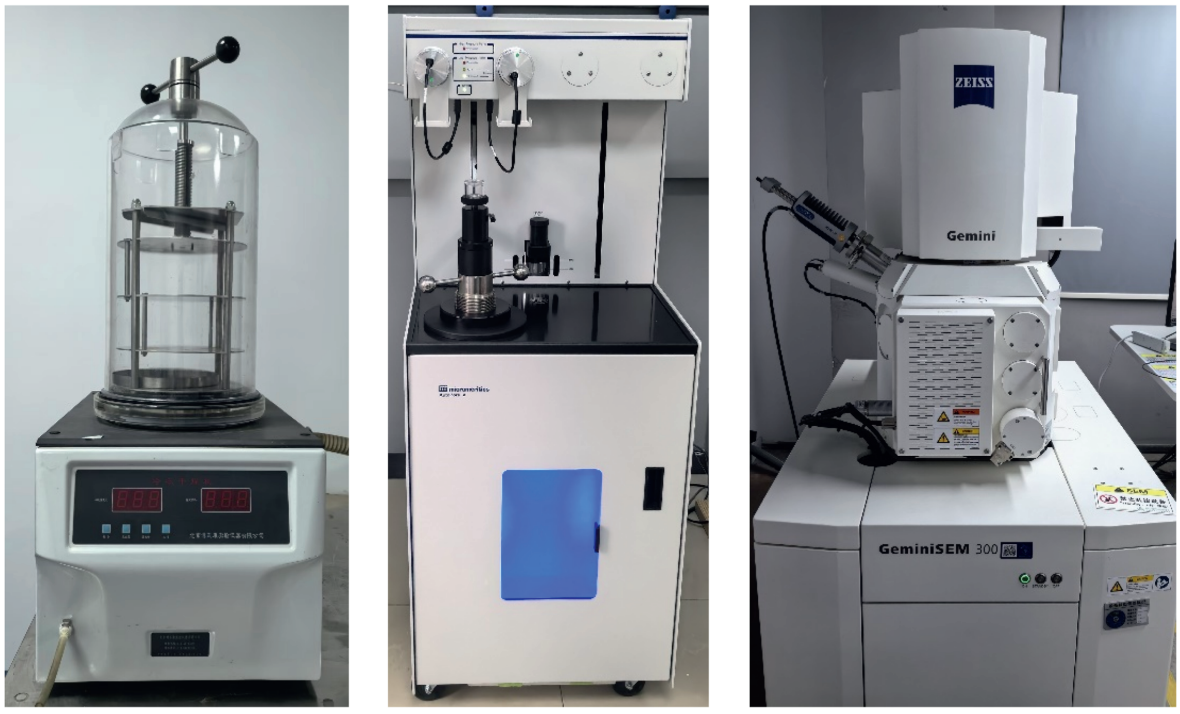

Fig. 6. The equipment of MIP and SEM: (a) Freeze dryer, (b) MIP, and (c) SEM.

In this study, SEM tests are conducted on freeze-dried specimens of six types of clays under four moisture conditions: saturated, dry, and two transitional states known as transition points 1 and 2, as shown in Fig. 7. Transition point 1 (w_1) represents the water content at the threshold between structural shrinkage and proportional shrinkage stages on the SSC. Conversely, transition point 2 (w_2) denotes the transition from proportional shrinkage to zero-shrinkage stages (Jia et al., 2024). For Yunnan and Longsheng clays, specimens with high water content experience significant fracturing after freeze-drying, rendering them unsuitable for placement into the SEM chamber. Therefore, SEM observations for these two clays are limited to three conditions: saturated, $w = w_2$, and dry states. These tests provide valuable insights into the microstructure and pore-size characteristics of clay specimens under drying conditions.

3. Results and discussion

3.1. Correlation between SSC and SWRC

Fig. 7 presents the SWRCs and SSCs of three high-plasticity clay specimens (Yunnan clay, Guilin clay and Longsheng clay) over a wide suction range, and the shrinkage data presented in Figs. 7 and 8 are sourced from Jia et al. (2024). As shown in Fig. 7, the SWRCs of all three clayey soils exhibit a bimodal distribution, while the SSCs display an S-shaped curve. Based on the shapes of the SWRC and SSC, both curves can be divided into three distinct stages (I-III). In the low-suction stage of SWRC (Stage I), when the suction exceeds the air-entry value, water in macropores of inter-aggregate matrix begins to drain, leading to a rapid decrease in water content. When the suction exceeds 40–60 kPa, the rate of pore water outflow decreases, indicating a reduction in the volume of pores corresponding to this suction range. As the suction continuously increases beyond 250–300 kPa for tested soils, the reduction rate of water content further becomes slow. This phenomenon can be attributed to two factors: (1) the small amount of remaining water in these pores corresponding to the applied suction and (2) the increasing connectivity of gas phase within the soils. The gas-phase connectivity inhibits the water-phase flow, making the drainage of pore water increasingly difficult (Bocking and Fredlund, 1980). Beyond this stage, the ATT becomes inapplicable. This also indicates that most of the pore water in macropores from the inter-aggregate matrix has already been expelled.

From Fig. 7, the low suction stage in the SWRC corresponds to the structural shrinkage phase in the SSC. One transition point between the structural shrinkage stage and the proportional shrinkage stage, as well as the onset of the zero-shrinkage phase, are labeled as w_1 and w_2, respectively (Jia et al., 2024). In stage I, the structural integrity of the soil prevents volume shrinkage during the transition from a saturated state to the complete drainage of macropore water. The gas-phase connectivity can be identified through the SWRC where macropore water is nearly completely drained out at w_1. As shown in Fig. 7a, at stages II and III, the SWRC demonstrates a rapid increase in suction with decreasing water content. An approximately linear relationship between suction and water content can be observed in a semi-logarithmic coordinate. Meanwhile, the SSC reveals a gradual decrease in void ratio as water content decreases, indicating soil shrinkage. When the water content reduces to 17 %, the increase rate of suction in the SWRC slows significantly, forming an inflection point. Simultaneously, the water content in the inflection point equals the one in the onset of the zero-shrinkage stage w_2 in the SSC, where the suction approaches 10 MPa. As the water content decreases to the dry state, the suction in soil specimens increases rapidly, and the soil remains in a nearly zero-shrinkage status.

Fig. 7b and c depicts the SWRCs of Guilin clay and Longsheng clay, both of which exhibit inflection points. These inflection points correspond to w_2 in stages II and III of SSC. Due to the differences in soil properties, the water contents corresponding to these transition points vary. For Guilin clay and Longsheng clay, the values of w_2 are 26 % and 22 %, respectively. The sequential drainage of pore water, from macropores in inter-aggregate matrix to micropores in intra-aggregate matrix, suggests that the drainage of water from micropores does not significantly induce soil shrinkage. The underlying mechanisms will be further investigated through microstructural experiments in subsequent section.

Fig. 8 presents the correlation between the SWRCs and SSCs of three low-plasticity specimens, including Yueyang clay, Sanmenxia clay, and Taizhou clay. The SWRC of Yueyang clay exhibits a bimodal morphology, while the SWRCs of Sanmenxia clay and Taizhou clay display unimodal morphology. In the stage I beyond the air-entry value, the macropore water in Yueyang and Sanmenxia clays begins to drain. As suction continuously increases, the drainage of pore water gradually slows. When the suction exceeds 250 kPa, the pore water drainage becomes minimal and time-consuming. The water content at approximately 300 kPa corresponds to the first transition point w_1 in the SSC, being consistent with the findings shown in Fig. 7. As the suction continues to increase and water content decreases further, the SWRC of Yueyang clay exhibits an inflection point when the water content reduces to 10 % where the SSC enters the stage III and similarly the suction approaches to 10 MPa. In contrast, this phenomenon is absent in Sanmenxia clay. Fig. 8c shows the correlation between the SWRC and SSC of Taizhou clay. Compared to other soils, the SWRC in Taizhou clay exhibits a smaller overall change in water content at stage I. Moreover, the structural shrinkage stage is not evident in the SSC. At stage II, as suction increases, the water content decreases steadily.

Unlike other soils, the SWRC of Taizhou clay does not exhibit an inflection point, and the zero-shrinkage phase in the SSC is also not apparent. This phenomenon may be attributed to the clay minerals present in clayey soils (Mitchell and Soga, 2005). As illustrated in Fig. 2, the content of illite/smectite mixed layer in Taizhou clay is notably high. It could be suggested that the second inflection point in the SWRC is related to the content of illite/smectite mixed layer. The presence of clay minerals enhances the soil's water retention capacity, enabling it to retain a larger quantity of water, even under high suction conditions. Consequently, significant volumetric shrinkage is observed in the SSC even at high suction levels. As a result, both the SSC and SWRC exhibit smoother transitions. These findings highlight the close relationship between the SWRC and SSC in clayey soils. There is consistency in the morphological characteristic water contents of the SWRC and SSC for all the tested clayey specimens. This study recognizes its limitations in considering the three-dimensional relationship among suction, water content, and volumetric deformation, as well as the multimodal features of SWRCs. The insights provided by Hu et al. (2013) and Yan et al. (2022) serve as valuable guides for future research.

3.2. The connection with PSD

Fig. 9 shows the PSD curves and cumulative mercury intrusion curves of six clayey soils. Fig. 9a–d shows that the four soils exhibit bimodal PSDs, consistent with the bimodal patterns observed in their SWRCs. The similar results have also been identified by Yan and Cudmani (2024). In contrast, the PSDs of Sanmenxia clay and Taizhou clay do not exhibit bimodal characteristics, which align with the unimodal patterns in their SWRCs.

In the case of Yunnan clay depicted in Fig. 9a, macropores

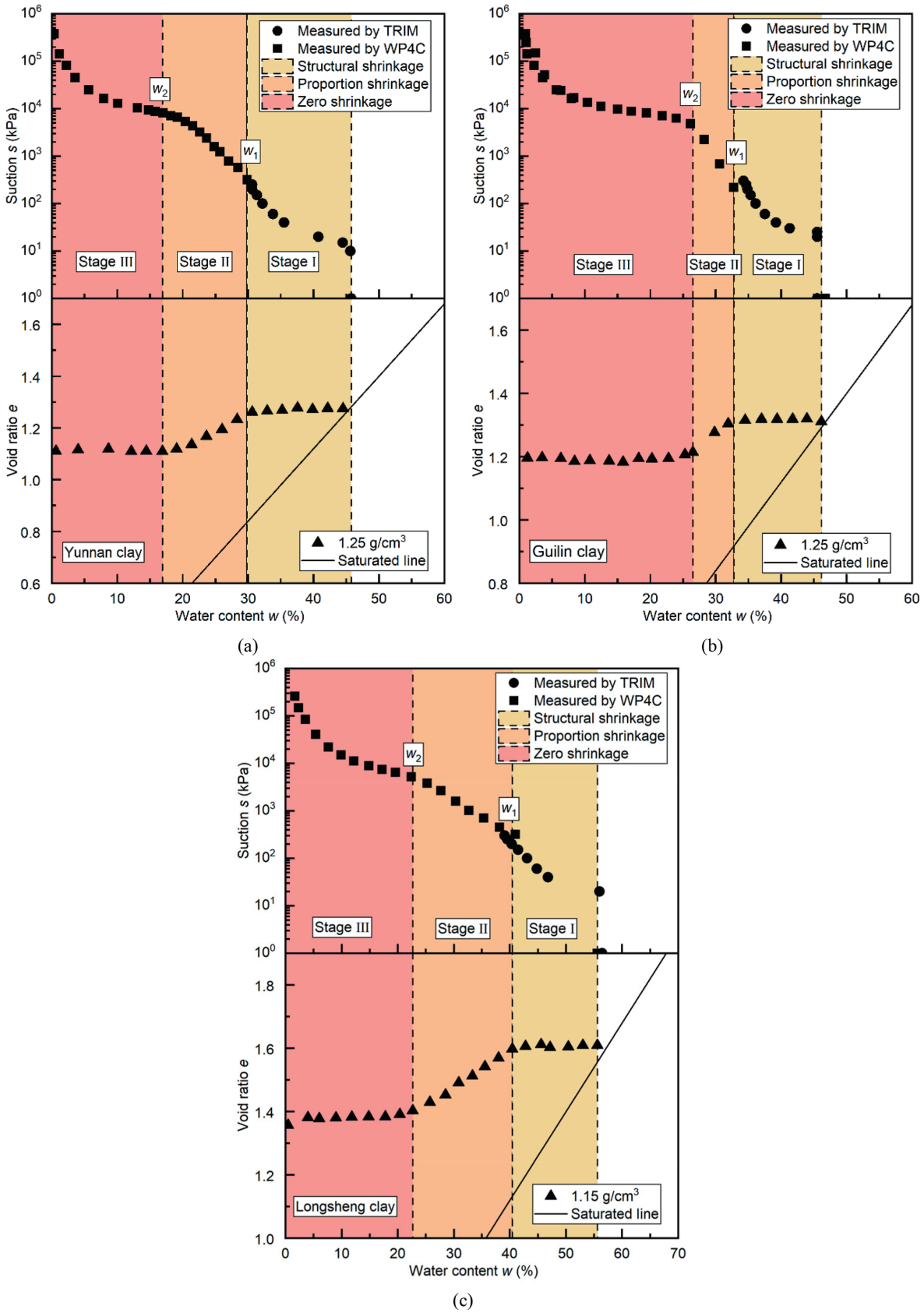

Fig. 7. The correlation between the SSCs and SWRCs of high-plasticity clay specimens: (a) Yunnan clay, (b) Guilin clay, and (c) Longsheng clay.

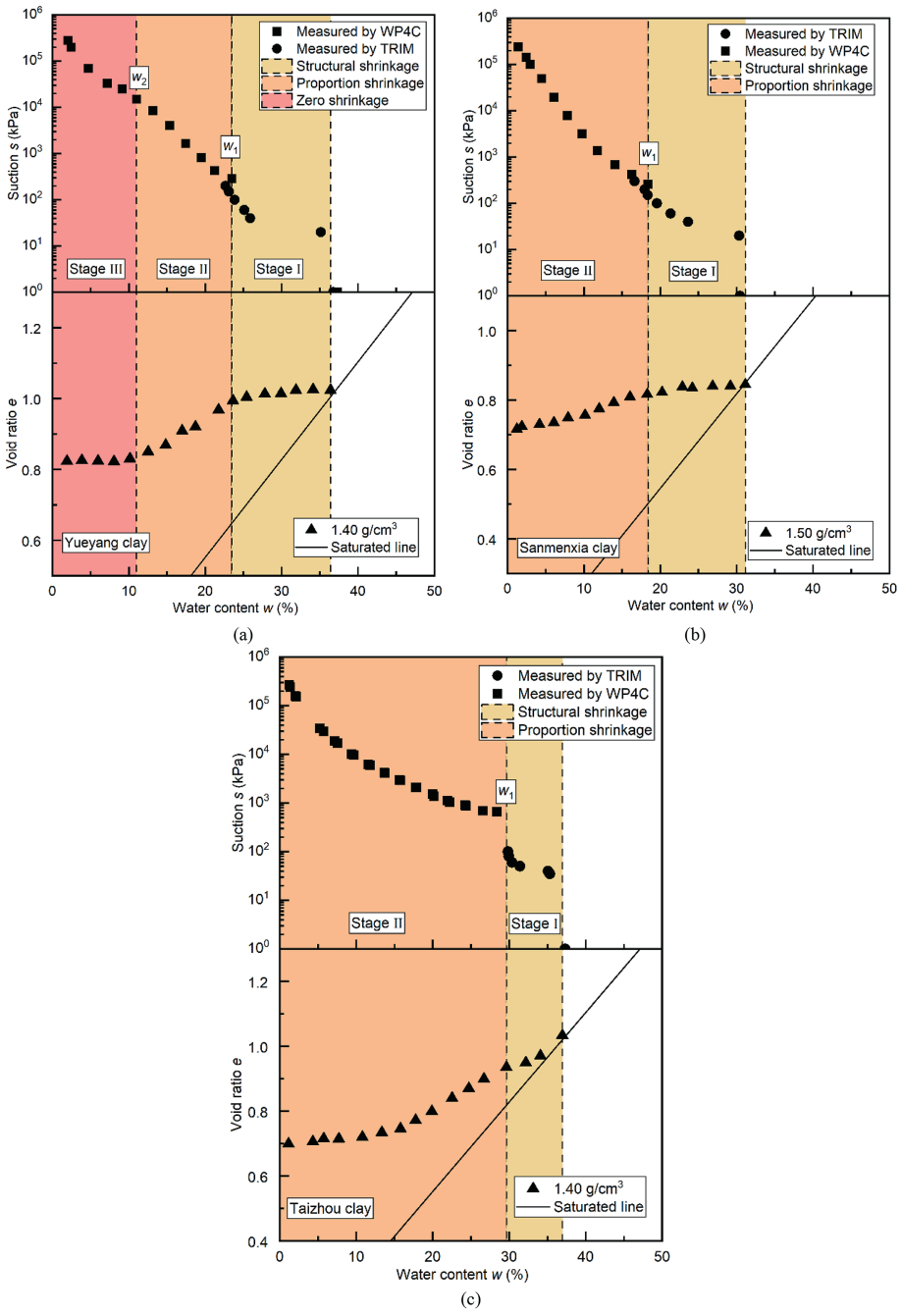

Fig. 8. The correlation between the SSCs and SWRCs of low-plasticity clay specimens: (a) Yueyang clay, (b) Sanmenxia clay, and (c) Taizhou clay.

correspond to the peak on the right side of the graph, representing pore sizes larger than 0.8 μm. It is noted that this is even smaller than the clay particle size of 2 μm. The distribution of mesopores in compacted Yunnan clay ranges from 0.1 to 0.8 μm, while micropores correspond to the left-side peak, indicating the pore sizes less than 0.1 μm. For other clayey soils, as shown in Fig. 9b–f, the smallest value for the macropore size is defined at 0.6 μm for Guilin clay, 3.4 μm for Longsheng clay, 0.3 μm for Yueyang clay, and 0.3 μm for Sanmenxia clay. However, Taizhou clay does not exhibit a clear demarcation boundary. Among these soils, Guilin clay exhibits the highest peak value for micropores, approximately 0.47 mL/g, while Yueyang clay shows the lowest peak value for micropores, approximately 0.1 mL/g. This observation corresponds to the extent of the zero-shrinkage phase in the SSC, indicating that the micropore proportion dominates the range of the zero-shrinkage phase. The zero-shrinkage phase refers to the stage when the pore water is drained from micropores and no further volumetric changes occur. However, Sanmenxia clay exhibits a low micropore content and the smallest cumulative mercury intrusion volume among the six soils. Hence, the lack of a distinct zero-shrinkage phase and the relatively small shrinkage deformation are observed in this clay specimen, consistent with their SSC and SWRC results. The PSD curve of Taizhou clay reveals that the macropore peak value is approximately 0.11 mL/g, the smallest among the six soils. This result corresponds to the absence of a distinct structural shrinkage phase. Additionally, the pores in

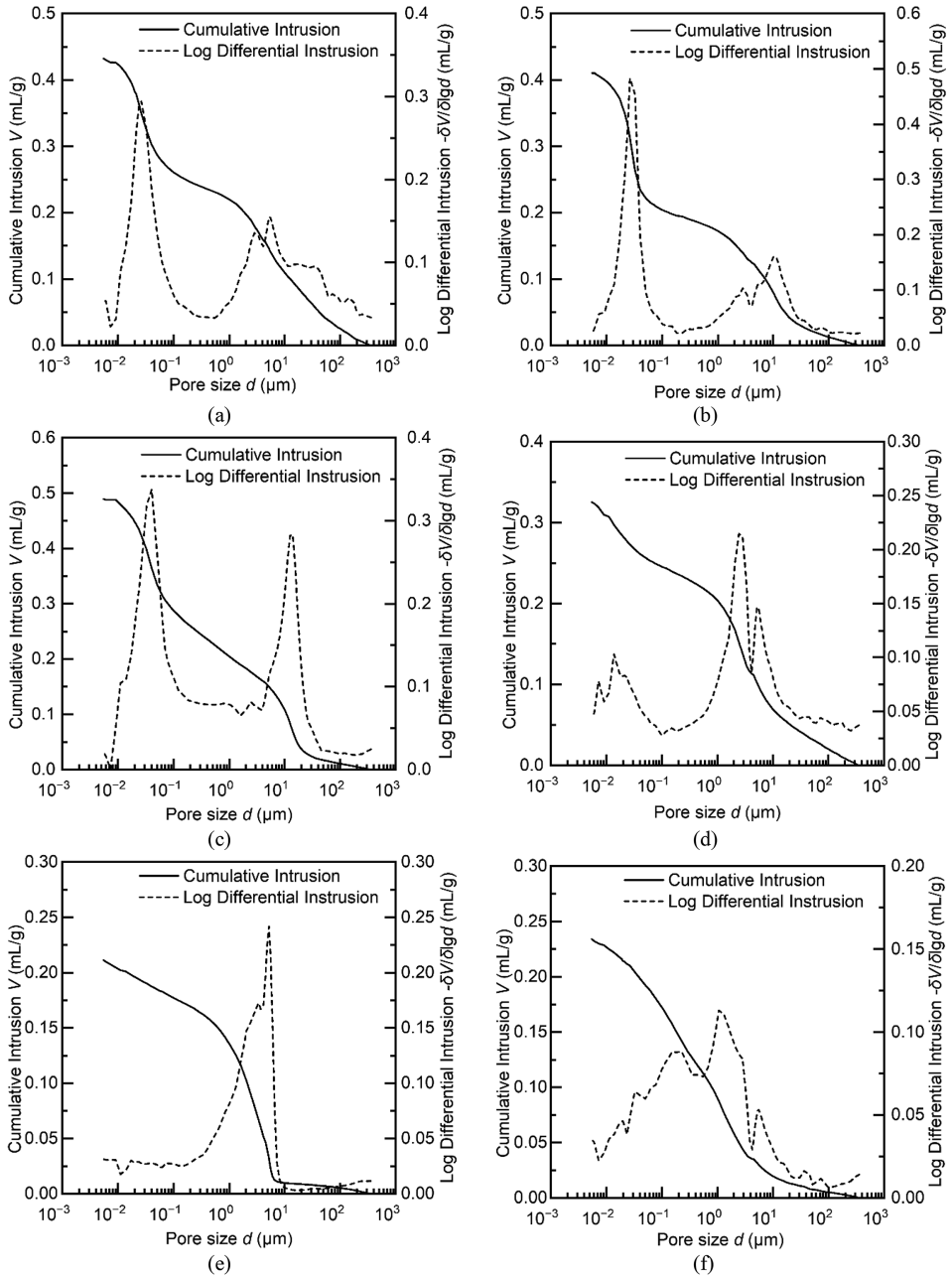

Fig. 9. Results of MIP tests on specimens: (a) Yunnan clay, (b) Guilin clay, (c) Longsheng clay, (d) Yueyang clay, (e) Sanmenxia clay, and (f) Taizhou clay.

Taizhou clay are primarily distributed within the mesopore range, with a low micropore content. The total shrinkage volume of Taizhou clay is the highest among the six soils, further confirming that the shrinkage volume of soil is controlled by the mesopore content. The low proportion of micropores within the clay predominantly accounts for the absence of a distinct zero-shrinkage phase in the SSC and the lack of an obvious inflection point in the SWRC. These findings highlight the correlation between soil microstructure and macroscopic behavior, indicating that the morphological characteristics of SWRCs and SSCs directly mirror the pore structure of soil.

3.3. Connection with microstructure of clay

Fig. 10a–j presents the SEM test results for Yunnan clay, Guilin clay, and Longsheng clay under different water content conditions. Due to the high-water content in soils, the freeze-drying process causes severe sample fragmentation, making sample preparation challenging. Consequently, SEM testing is not conducted for Yunnan clay and Longsheng clay at the water content corresponding to w_1. The SEM results for the saturated state are shown in Fig. 10a–d, and h. Under saturated conditions, soil particle aggregates are scarce, and the aggregation phenomenon is not pronounced. Hence, the PSD is relatively uniform.

Fig. 10e shows the SEM results for Guilin clay when the water content is reduced to w_1. The results indicate that soil particle aggregates increase and inter-aggregate pores emerge. During this stage, from saturation to w_1 during the drying process shown in Fig. 7b, limited shrinkage of the soil is observed, indicating that the formation of aggregates does not lead to significant volumetric

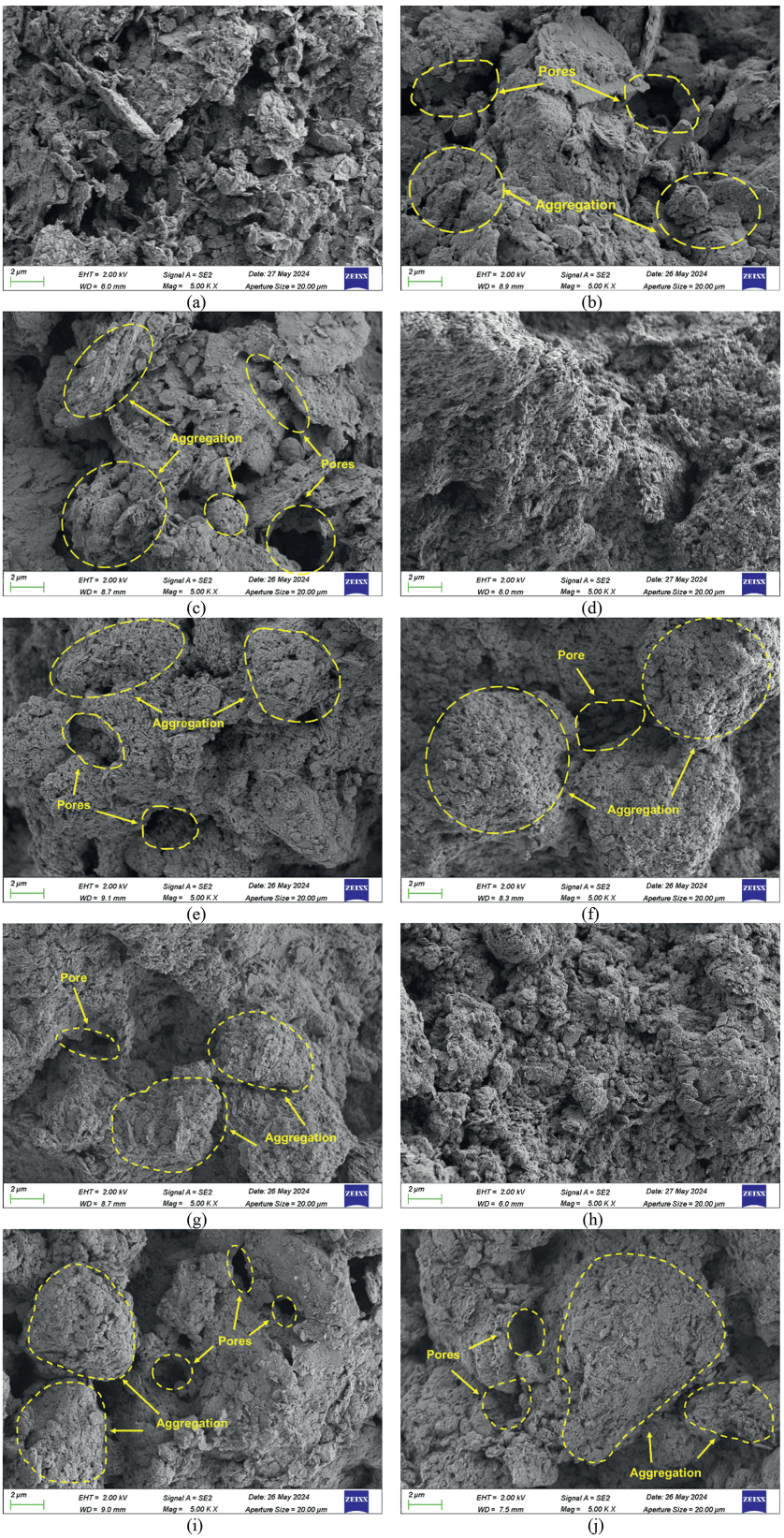

Fig. 10. SEM results of soils: (a) Saturated - Yunnan clay, (b) $w_2 = 16.9$ % - Yunnan clay, (c) $w = 0$ % - Yunnan clay, (d) Saturated – Guilin clay, (e) $w_1 = 32.8$ % – Guilin clay, (f) $w_2 = 26.5$ % – Guilin clay, (g) $w = 0$ % – Guilin clay, (h) Saturated - Longsheng clay, (i) $w_2 = 22.7$ % - Longsheng clay, and (j) $w = 0$ % - Longsheng clay.

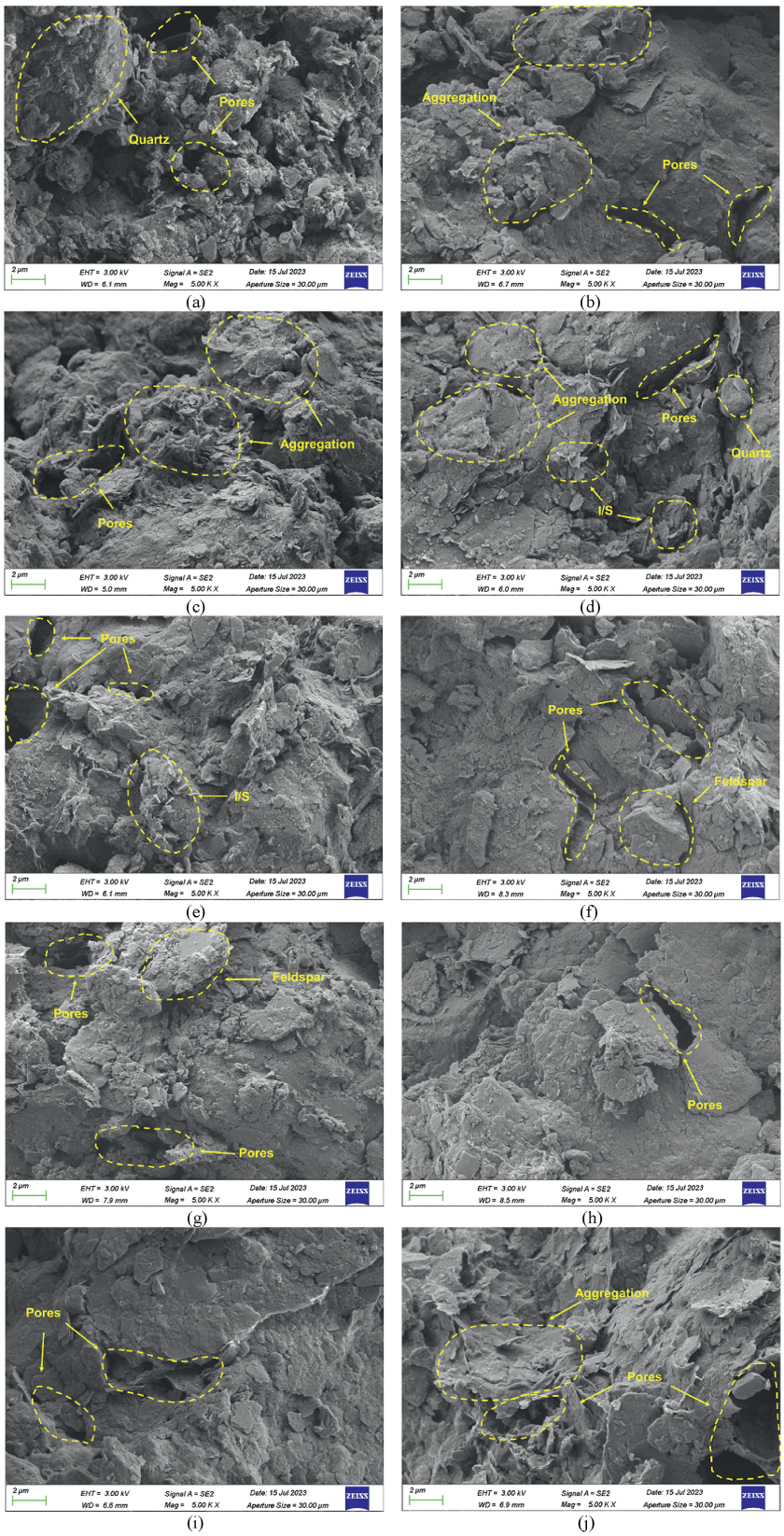

Fig. 11. The SEM observations of soils: (a) Saturated - Yueyang clay, (b) $w_1 = 26.2$ % - Yueyang clay, (c) $w_2 = 9.8$ % - Yueyang clay, (d) $w = 0$ % - Yueyang clay, (e) Saturated - Sanmenxia clay, (f) $w_1 = 21.2$ % - Sanmenxia clay, (g) $w_2 = 5$ % - Sanmenxia clay, (h) $w = 0$ % - Sanmenxia clay, (i) Saturated - Taizhou clay, (j) $w_1 = 30$ % - Taizhou clay, (k) $w_2 = 8$ % - Taizhou clay, and (l) $w = 0$ % - Taizhou clay.

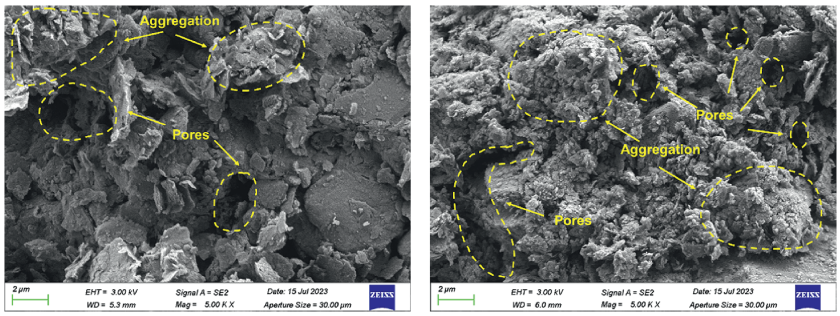

(k) (l)

Fig. 11. (*continued*).

changes in the soil. The SEM results at water content of w_2 are shown in Fig. 10b-f, and i. At this stage, the aggregation phenomenon becomes more pronounced, and the inter-aggregate pores obviously diminish compared to the state at water content of w_1. This finding suggests that the soil shrinkage is caused by the reduction of inter-aggregate pores. These pores correspond to mesopores and macropores, which are consistent with the results from Fig. 9a–c. Fig. 10c–g, and j illustrates the SEM results for the three soils under completely dry conditions. Compared to the state at w_2, no significant changes in aggregate pore size are observed, suggesting that during the zero-shrinkage phase, pore water is expelled from within the aggregates. The change in water content within the aggregates results in insignificant volumetric changes in the soil. The results of Fig. 9a–c and 10 provide direct microscopic evidence of the relationship between soil pore structure and shrinkage behavior, demonstrating that the soil shrinkage primarily originates from changes in inter-aggregate pore sizes rather than from changes within the aggregates themselves.

Fig. 11 presents the SEM results for Yueyang clay, Sanmenxia clay, and Taizhou clay under different states, including saturated, transition points (w_1, w_2) and completely dry conditions. The SEM results of the three soils under saturated conditions are also shown in Fig. 11a-e, and i. The results indicate that soil particles are evenly distributed, loosely arranged, and exhibit numerous pores with no significant aggregation phenomena. Since Taizhou clay lacks a distinct structural shrinkage phase, Fig. 11j presents its SEM results at the unsaturated state. The distribution of soil particles remains relatively uniform, with fewer aggregates and no significant separation between aggregates. Due to the low strength of the soil skeleton, the soil volume decreases along the saturation line during water loss. Fig. 11b and f shows the SEM results for the water content reduced to w_1. During the desaturation process from saturation to w_1, water is expelled from macropores, and soil particles exhibit aggregation. At this stage of Fig. 8a and b and 9d, e, inter-aggregate pores emerge, but the soil volume does not change significantly, indicating that only a very slight volumetric change occurred at the macroscopic level. Fig. 11c–g, and k shows the SEM results when the water content is further reduced to w_2. At this stage, the aggregation phenomenon becomes more pronounced. The increase in effective stress between particles reduces the inter-aggregate pore size, transforming macropores into mesopores, which macroscopically manifests as soil shrinkage. At $w = 0$ %, the SEM results reveal that the micropores within aggregates increase, while no significant changes occur in the inter-aggregate pores. The findings depicted in Fig. 8, alongside Fig. 9d–f and 11, further confirm the observation that changes within the micropores of aggregates do not lead to perceptible soil shrinkage. Instead, soil shrinkage is driven by the reduction of inter-aggregate pores.

To further validate the experimental findings, both the volumetric changes of inter-aggregate and intra-aggregate pores are quantified. For the six types of clayey soils, listed sequentially in Table 1, the proportions of total deformation caused by water loss attributable to changes in inter-aggregate pore volume are 94.5 %, 91.1 %, 86.6 %, 96.3 %, 89.5 %, and 93.6 %, respectively. These findings provide further microscopic evidence that the soil shrinkage behavior is predominantly controlled by changes in inter-aggregate pore structures. Conversely, internal structural changes within aggregates have a negligible impact on the overall soil volume change.

4. Conclusions

The correlation between SWRC and SSC of clayey soils remains largely unexplored. Moreover, the hydraulic and mechanical behavior at the representative elementary volume (REV) scale is rarely linked to the pore structure evolution at the pore scale under drying conditions. To address this gap, a series of soil-water retention and soil shrinkage tests is conducted over a wide suction range on six types of compacted clays. These tests employ a combination of the axis-translation technique and RH control method. Furthermore, the evolutions of PSD and microstructure within these clays are meticulously measured using the MIP and SEM methods. A thorough investigation into the underlying mechanisms connecting the SWRC and SSC at the two different scales is performed. The main conclusions drawn from this study are as follows:

(1) The morphological characteristics of SWRC and SSC show considerable consistency, indicating a strong relationship between soil-water retention and soil shrinkage behavior. In the low suction range, pore water in compacted clayey specimens begins to drain from macropores. However, as suction increases, the drainage of pore water is hindered by the limited water content within the corresponding pores and the interconnectivity of the gas phase, making the axis-translation technique inapplicable. The SWRC in the low suction range is identified as an indicator of the structural shrinkage stage of SSC. A distinct inflection point in the SWRC in a high suction range signifies the onset of the zero-shrinkage stage in the SSC. Moreover, the characterized water contents in pores for both SWRC and SSC are identified. There is noted consistency between the bimodal distributions of pore size derived from MIP and the bimodal morphology of the SWRC. The proportion and arrangement of micropores significantly influence the bimodal characteristics of the SWRC and define the span of the zero-shrinkage phase in soils. SEM results indicate that the primary volume change in soil shrinkage comes from the modification of inter-aggregate pores during drying.

Conversely, the evolution of intra-aggregate pores has minimal impact on the shrinkage of compacted clayey soils.

(2) Although the connection between the hydraulic and mechanical behavior and pore structure evolution is explored in depth based on the experimental results, the quantitative analysis that integrates both the REV-scale and pore-scale remains limited through this study. This limitation could potentially be addressed by transferring the PSD to SWRC and considering the effect of clay minerals. This should be prioritized in future research. However, the current findings significantly enhance our comprehension of the interplay between the hydraulic and mechanical behavior of compacted clays in the drying process. Additionally, the results present a valuable potential for determining both the SWRC and SSC using the PSD of clayey soils.

CRediT authorship contribution statement

Sheng'ao Jia: Writing – original draft, Resources, Investigation, Data curation. **De'an Sun:** Writing – review & editing, Validation, Supervision, Project administration, Funding acquisition. **Pan Chen:** Writing – review & editing, Supervision, Funding acquisition, Conceptualization.

Declaration of competing interest

The authors declare that they have no known competing financial interests or personal relationships that could have appeared to influence the work reported in this paper.

Acknowledgments

This research was supported by the National Natural Science Foundation of China (Grant Nos. 52238007 and 52378354), the Research Fund Key Laboratory of Geomechanics and Geotechnical Engineering Safety, Chinese Academy of Sciences (Grant No. JBGS2405), and the Science and Technology Program of Guizhou Department of Transportation (Grant No. 2023-122-035).

References

ASTM D854-23, 2023. Test Methods for Specific Gravity of Soil Solids by Water Pycnometer. ASTM International, West Conshohocken, USA.
ASTM D4318-17e1, 2018. Standard Test Methods for Liquid Limit, Plastic Limit, and Plasticity Index of Soils. ASTM International, West Conshohocken, PA, USA.
ASTM D7928-21e1, 2021. Standard Test Method for Particle-Size Distribution (Gradation) of Fine-Grained Soils Using the Sedimentation (Hydrometer) Analysis. ASTM International, West Conshohocken, PA, USA.
ASTM D2487-17e1, 2018. Standard Practice for Classification of Soils for Engineering Purposes (Unified Soil Classification System). ASTM International, West Conshohocken, PA, USA.
ASTM F3419-22, 2022. Standard Test Method for Mineral Characterization of Equine Surface Materials by X-Ray Diffraction (XRD) Techniques. ASTM International, West Conshohocken, PA, USA.
ASTM D6836-16, 2016. Standard Test Methods for Determination of the Soil Water Characteristic Curve for Desorption Using Hanging Column, Pressure Extractor, Chilled Mirror Hygrometer, or Centrifuge. ASTM International, West Conshohocken, PA, USA.
ASTM E104-20a, 2020. Standard Practice for Maintaining Constant Relative Humidity by Means of Aqueous Solutions. ASTM International, West Conshohocken, PA, USA.
Bocking, K.A., Fredlund, D.G., 1980. Limitations of the axis-translation technique. In: Fourth International Conference on Expansive Soils, pp. 1–19. Denver, CO, USA.
Bore, T., Mishra, P.N., Wagner, N., et al., 2021. Coupled hydraulic, mechanical and dielectric investigations on kaolin. Eng. Geol. 294, 106352.
Chen, P., Jia, S., Wei, X.Q., Sun, P.P., Yi, P.P., Wei, C.F., 2023. Hydraulic path dependence of shear strength for compacted loess. J. Rock Mech. Geotech. Eng. 15 (7), 1872–1882.
Chen, P., Lu, N., 2018. Generalized equation for soil shrinkage curve. J. Geotech. Geoenviron. Eng. 144 (8), 04018046.
Chen, P., Wei, C.F., Ma, T.T., 2015. Analytical model of soil-water characteristics considering the effect of air entrapment. Int. J. GeoMech. 15 (6), 04014102.
Chen, P., Wei, C.F., Yi, P.P., Ma, T.T., 2017. Determination of hydraulic properties of unsaturated soils based on nonequilibrium multistep outflow experiments. J. Geotech. Geoenviron. Eng. 143 (1), 04016087.
Fredlund, D.G., 2019. State of practice for use of the soil-water characteristic curve (SWCC) in geotechnical engineering. Can. Geotech. J. 56 (8), 1059–1069.
Fredlund, M.D., Wilson, G.W., Fredlund, D.G., 2002. Representation and estimation of the shrinkage curve. In: Juca, J.F.T., de Campos, T.M.P., Marinho, F.A.M. (Eds.), Proceedings of the 3rd International Conference on Unsaturated Soils (UNSAT 2002). CRC Press, London, British, pp. 145–149.
Gao, Y., Sun, D.A., 2017. Soil-water retention behavior of compacted soil with different densities over a wide suction range and its prediction. Comput. Geotech. 91, 17–26.
Gillott, J., 1976. Importance of specimen preparation in microscopy. In: Sangrey, D.A., Mitchell, R.J. (Eds.), Soil Specimen Preparation for Laboratory Testing, STP599-EB. ASTM International, Philadelphia, PA, USA, pp. 289–307.
Gupt, C.B., Prakash, A., Hazra, B., Sreedeep, S., 2022. Predictive model for soil shrinkage characteristic curve of high plastic soils. Geotech. Test. J. 45 (1), 101–124.
Haines, W.B., 1923. The volume-changes associated with variations of water content in soil. J. Agric. Sci. 13 (3), 296–310.
Hu, R., Chen, Y.F., Liu, H.H., Zhou, C.B., 2013. A water retention curve and unsaturated hydraulic conductivity model for deformable soils: consideration of the change in pore-size distribution. Geotechnique 63 (16), 1389–1405.
Jain, S., Wang, Y.H., Fredlund, D.G., 2015. Non-contact sensing system to measure specimen volume during shrinkage test. Geotech. Test. J. 38 (6), 936–949.
Jia, S., Chen, P., Wei, C.F., Tian, H.H., Yi, P.P., 2024. The connection between soil shrinkage and pore water distribution of compacted clays using the nuclear magnetic resonance technique. Acta Geotech 19, 6039–6054.
Krisdani, H., Rahardjo, H., Leong, E.C., 2008. Effects of different drying rates on shrinkage characteristics of a residual soil and soil mixtures. Eng. Geol. 102 (1–2), 31–37.
Leroueil, S., 2001. Natural slopes and cuts: movement and failure mechanisms. Geotechnique 51 (3), 197–243.
Lin, B.T., Cerato, A.B., 2013. Hysteretic soil water characteristics and cyclic swell–shrink paths of compacted expansive soils. Bull. Eng. Geol. Environ. 72, 61–70.
Lu, N., Likos, W.J., 2004. Unsaturated Soil Mechanics. John Wiley, Hoboken, NJ, USA.
Lu, N., Wayllace, A., Carrera, J., Likos, W.J., 2006. Constant flow method for concurrently measuring soil-water characteristic curve and hydraulic conductivity function. Geotech. Test. J. 29 (3), 230–241.
Ma, T.T., Wei, C.F., Yao, C.Q., Yi, P.P., 2020. Microstructural evolution of expansive clay during drying–wetting cycle. Acta Geotech 15 (8), 2355–2366.
Marinho, F.A.M., 2018. Fundamentals of soil shrinkage. In: Hoyos, L.R., McCartney, J.S., Houston, S.L., Likos, W.J. (Eds.), Proceedings of the 2nd Pan-American Conference on Unsaturated Soils. ASCE, Reston, VA, USA.
Mitchell, J., Soga, K., 2005. Fundamentals of Soil Behavior, third ed. John Wiley, Hoboken, NJ, USA.
Mishra, P.N., Bore, T., Jiang, Y., Scheuermann, A., Li, L., 2018. Dielectric spectroscopy measurements on kaolin suspensions for sediment concentration monitoring. Measurement 121, 160–169.
Mishra, P.N., 2020. Soft soil characterisation and improvement for reclaimed land application. School of Civil Engineering. The University of Queensland, Brisbane, Queensland, Australia. PhD Thesis.
Moore, D.M., Reynolds Jr., R.C., 1997. X-ray Diffraction and the Identification and Analysis of Clay Minerals. Oxford University Press, New York, NY, USA.
Peng, X.H., Horn, R., 2005. Modeling soil shrinkage curve across a wide range of soil types. Soil Sci. Soc. Am. J. 69 (3), 584–592.
Saha, A., Sekharan, S., 2021. Importance of volumetric shrinkage curve (VSC) for determination of soil–water retention curve (SWRC) for low plastic natural soils. J. Hydrol. 596, 126113.
Salager, S., Nuth, M., Ferrari, A., Laloui, L., 2013. Investigation into water retention behaviour of deformable soils. Can. Geotech. J. 50 (2), 200–208.
Schwing, M., Chen, Z., Scheuermann, A., Williams, D.J., Wagner, N., 2014. Experimental study on the relationship of mechanic and hydraulic state variables, and the dielectric properties of clays. In: Khalili, N., Russell, A., Khoshghalb, A. (Eds.), Proceedings of the 6th International Conference on Unsaturated Soils (UNSAT 2014). CRC Press/Balkema, Leiden, Netherlands, pp. 247–253.
Schwing, M., 2016. Mechanical, hydraulic, and dielectric characterisation of fine-grained soils during densification. School of Civil Engineering. The University of Queensland, Brisbane, Australia. PhD Thesis.
Shi, B., Wu, Z., Inyang, H., Chen, J., Wang, B., 1999. Preparation of soil specimens for SEM analysis using freeze-cut-drying. Bull. Eng. Geol. Environ. 58, 1–7.
Song, Z.Y., Zhang, Z.H., Du, X.L., 2023. NMR-based analysis of pore water state of unsaturated compacted bentonite considering the saline effect. Geomech. Energy Environ. 33, 100441.
Song, Z.Y., Zhang, Z.H., Lu, Y.Q., Du, X.L., 2024. Shrinkage behavior of compacted bentonite considering physicochemical effects. Sci. Total Environ. 906, 167547.
Sun, D.A., Liu, W.J., Lyu, H.B., 2014. Soil-water characteristic curve of Guilin lateritic clay. Rock Soil Mech. 35 (12), 3345–3351.
Tian, H.H., Wei, C.F., Lai, Y.M., Chen, P., 2018. Quantification of water content during freeze–thaw cycles: a nuclear magnetic resonance based method. Vadose Zone J. 17, 160124.
Tian, H.H., Wei, C.F., Wei, H.Z., Yan, R.T., Chen, P., 2014. An NMR-based analysis of

soil–water characteristics. Appl. Magn. Reson. 45, 49–61.
Tian, H.H., Wei, C.F., 2020. Characterization and quantification of pore water in clays during drying process with low-field NMR. Water Resour. Res. 56 (10), e2020WR027537.
Wang, J.P., Liu, T.H., Wang, S.H., Luan, J.Y., Dadda, A., 2023. Investigation of porosity variation on water retention behaviour of unsaturated granular media by using pore scale Micro-CT and lattice Boltzmann method. J. Hydrol. 626, 130161.
Wayllace, A., Lu, N., 2012. A transient water release and imbibitions method for rapidly measuring wetting and drying soil water retention and hydraulic conductivity functions. Geotech. Test. J. 35 (1), 103–117.
Wei, C.F., Dewoolkar, M.M., 2006. A continuum theory of nonequilibrium two-phase flow through porous media with capillary relaxation. In: Lu, N., Hoyos, L.R., Reddi, L. (Eds.), Advances in Unsaturated Soil, Seepage, and Environmental Geotechnics - Proceedings of Sessions of the GeoShanghai Conference. ASCE, Reston, VA, USA, pp. 246–254.
Wen, T.D., Wang, P.P., Shao, L.T., Guo, X.X., 2021. Experimental investigations of soil shrinkage characteristics and their effects on the soil water characteristic curve. Eng. Geol. 284, 106035.
White, D.J., Take, W.A., Bolton, M.D., 2003. Soil deformation measurement using particle image velocimetry (PIV) and photogrammetry. Geotechnique 53 (7), 619–631.
Yan, G.X., Li, Z., Torres, S.A.G., Scheuermann, A., Li, L., 2022. Transient two-phase flow in porous media: a literature review and engineering application in geotechnics. Geotechnics 2 (1), 32–90.
Yan, W., Cudmani, R., 2024. A novel framework for deriving water retention behavior of multimodal unsaturated soils based on pore size distribution data. Acta Geotech 19, 8071–8088.
Yao, C.Q., Wei, C.F., Ma, T.T., Chen, P., Tian, H.H., 2021. Experimental investigation on the influence of thermochemical effect on the pore-water status in expansive soil. Int. J. GeoMech. 21 (6), 04021080.
Yin, S., Huang, J.N., Li, X.M., Bai, L.J., Zhang, X.W., Li, C.Q., 2022. Experimental study on deformation characteristics and pore characteristics variation of granite residual soil. Sci. Rep. 12, 12314.
Zhang, X.W., Liu, X.Y., Gao, H.D., Wang, G., An, R., Liang, Z., 2023. Impact of mica on geotechnical behavior of weathered granitic soil using macro and micro investigations. J. Rock Mech. Geotech. Eng. 16 (6), 2250–2266.
Zhou, B.C., Lu, N., 2021. Correlation between atterberg limits and soil adsorptive water. J. Geotech. Geoenviron. Eng. 147 (2), 04020162.

Prof. De'an Sun received his PhD in the field of geotechnical engineering from Nagoya Institute of Technology, Japan in 1994 and is currently a Professor in the Department of Civil Engineering at Shanghai University. His primary research interests include unsaturated soil mechanics and constitutive modeling of soils. He has been listed as one of Elsevier's Most Cited Chinese Researchers for several consecutive years (2020 to present). In 2023, he was selected as the keynote speaker for the 26th Huang Wenxi Lecture. He was awarded the Second Prize of the 2023 National Natural Science Award (ranked second), and has received 5 first-class or second-class prizes of natural science from the Ministry of Education or the Shanghai Municipal Government as the first or one of the top three contributors.